

# Prospective Dynamic 3D MRI Reconstruction via Latent-Space Motion Tracking from Single Measurement

Lixuan Chen Zhongnan Liu Jesse Hamilton James M. Balter Jeong Joon Park<sup>†</sup> Liyue Shen<sup>†</sup>  
University of Michigan

## Abstract

Prospective reconstruction is crucial in many clinical applications such as MRI-guided radiotherapy, which demands accurate image reconstruction and fast motion estimation from currently acquired measurements. However, prospective reconstruction remains challenging due to ultra-sparse sampling and stringent latency requirements. In this work, we propose PDMR, a **Prospective Dynamic 3D MRI Reconstruction** framework with latent-space motion tracking. Our core idea is to learn an efficient and generalizable latent manifold of motion fields offline, enabling rapid online adaptation for prospective reconstruction. Specifically, we parameterize the deformation vector fields (DVF) on a low-dimensional manifold, effectively reducing the search space for fast online adaptation, and employ a tri-plane representation to achieve geometry-aware and memory-efficient encoding of 3D motion. Experiments on both XCAT digital phantoms and in-house abdominal MRI datasets demonstrate that PDMR achieves high-fidelity and temporally consistent reconstruction across multiple prospective scenarios (Immediate and After-2min), outperforming state-of-the-art retrospective and online methods. Our results suggest a promising pathway toward ultra-fast, motion-aware prospective MRI reconstruction in clinical practice.

## 1. Introduction

In radiotherapy or interventional procedures, real-time visualization of 3D patient anatomy and accurate motion estimation are essential for enhancing treatment precision, as they directly guide therapeutic decisions [19]. Motivated by this need, our goal is to reconstruct images directly from instantaneously sampled ultra-sparse measurements acquired within the current latency window, known as *prospective reconstruction*.

In recent years, MR-guided treatment, where magnetic resonance imaging (MRI) is used to guide radiotherapy pro-

<sup>†</sup>Co-corresponding senior authors who supervise this work together.

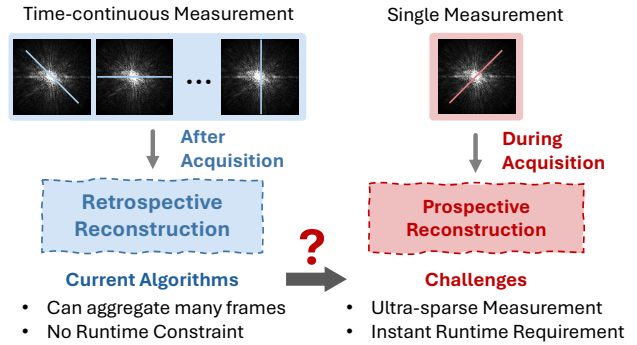


Figure 1. Retrospective methods face challenges in prospective reconstruction.

cedure of cancer patients to mitigate the motion effects such as respiration, has increasingly been recognized as an advanced clinical option [14]. Although MRI offers unparalleled soft-tissue contrast and non-invasive advantages, its inherently long acquisition time fundamentally limits the number of measurements that can be acquired within the allowed latency window for motion tracking. The resulting ultra-sparse sample makes prospective reconstruction problem highly ill-posed. Consequently, most previous works [5, 10, 30] focus on *retrospective reconstruction*, where dynamic images are reconstructed from time-continuous measurements after acquisition by aggregating all time frames together for a joint dynamic reconstruction, leveraging the spatio-temporal redundancy.

However, existing retrospective approaches cannot satisfy the demands of ultra-fast, low-latency prospective reconstruction, due to the significant challenges of ultra-sparse measurement and instant runtime requirement in the setting of prospective reconstruction, as shown in Fig. 1. On the other hand, the retrospective reconstruction has learned informative spatial-temporal representations offline for the specific patient, which naturally offers an important prior for prospective reconstruction of the same patient. Therefore, a key question arises: *how can we leverage the rich priors learned from retrospective reconstruction to enable low-latency prospective reconstruction from ultra-sparse*

*measurement (i.e., a single-shot k-space measurement)?* This overarching question can be further divided into two sub-problems: (a) How can we learn a good retrospective prior? (b) How can we rapidly adapt this prior for low-latency prospective reconstruction?

**How to learn a good retrospective prior?** Although retrospective reconstruction can exploit the full spatio-temporal redundancy across all time frames, learning a powerful prior from undersampled dynamic measurements still remains a very challenging problem. One promising direction is motion-compensated (MoCo) representation [18, 20, 21, 28], which explicitly decompose the dynamic sequence into a time-dependent deformation vector field (DVF) and a static template image. This decomposition allows the entire image sequence to share the same spatial structure and effectively exploit the spatio-temporal redundancy in the acquired measurements, leading to improved reconstruction quality. Clinically, patients often undergo multiple scans across treatment fractions. The MoCo decomposition naturally allows the template image to be obtained from a pre-scan or a previous fraction, providing high-quality patient-specific structural information as a prior, further alleviating the ill-posedness.

**How can we rapidly adapt this prior for low-latency prospective reconstruction?** With the MoCo decomposition, prospective reconstruction reduces to learning a patient-specific motion representation that can be quickly adapted to a new motion status at each new time point. Recent methods attempt to address this. MR-MOTUS [13] and DREME-MR [25] model deformation vector fields (DVFs) as a *linear* combination of spatial and temporal bases, enabling compact motion representations from undersampled measurements. During prospective reconstruction, they reuse retrospectively learned spatial bases and update only the temporal coefficients, allowing efficient online adaptation. However, because linear bases cannot capture the complex, nonlinear anatomical motion seen in practice, their representational limits reduce accuracy and robustness under ultra-sparse sampling. Prior-ISR [16] takes a different strategy by defining a discrete prior space spanning representative respiratory states. Online reconstruction searches this space to find the prior that best matches the incoming measurement. While effective under simplified motion patterns, this handcrafted and discrete manifold does not generalize well and fails to reflect the continuous nature of physiological motion, limiting its clinical applicability.

In this work, we propose **PDMR**, which is, to the best of our knowledge, the *first* Prospective Dynamic MRI Reconstruction framework that leverages a non-linear manifold-based deformation representation. To enable effective adaptation from a single measurement during

prospective reconstruction, we first retrospectively learn a compact and temporally generalizable latent space that can capture the underlying dynamics of deformation fields. Specifically, we incorporate a geometry-aware mapping network based on the tri-plane representations [4] to learn a nonlinear mapping from the latent manifold to full 3D DVFs. The tri-plane representation provides a high-resolution and structurally coherent feature embedding, allowing the model to preserve both global anatomy and fine local deformation details. This results in a strong retrospective prior that makes fast and stable DVF adaptation feasible during prospective reconstruction.

Benefiting from the compact manifold and the generalizable mapping network, PDMR can efficiently and accurately estimate the current DVF from instantaneous measurements (*i.e.*, a single spoke). During prospective reconstruction, PDMR only needs to optimize a low-dimensional latent vector on the learned manifold, requiring just a few iterations to recover the current motion state and produce high-quality images. Experiments on both XCAT digital phantoms [24] and in-house abdominal MRI datasets demonstrate that PDMR achieves high-fidelity reconstruction and accurate motion tracking across multiple prospective scenarios, confirming the effectiveness and generalizability of manifold-based DVF modeling.

To summarize, our key contributions are as follows:

- We introduce PDMR, the first framework that leverages a retrospectively learned, patient-specific motion manifold that can rapidly adapt to the latency window, enabling high-quality prospective reconstruction from instantaneous measurements.
- We propose a new geometry-aware manifold mapping network tailored to estimate a fine-grained time-varying deformation field from ultra-sparse measurements.
- We evaluate PDMR extensively, showing superior reconstruction quality and robustness to diverse motions across multiple prospective MR scenarios.

## 2. Related Work

### 2.1. Manifold Learning in Medical Imaging

Manifold learning has been widely used to capture the low-dimensional structure underlying high-dimensional medical images. Classical nonlinear methods such as LLE [23], Laplacian Eigenmaps [2], and diffusion maps [7] have been applied to analyze anatomical shape variability and deformation field [13, 25]. With deep learning, generative models, including VAEs [15] and latent-variable motion models for cardiac and respiratory dynamics [1], learn smooth latent spaces that capture physiological states [3]. These representations have enabled tasks such sparse-view reconstruction, or motion modeling from limited observations.

More recently, implicit neural representations (INRs)

have emerged as continuous neural manifolds for encoding anatomy and motion [16, 17, 22, 26, 27]. INR-based models [8] have been used for volumetric MRI reconstruction and deformation modeling, but most operate retrospectively or depend on fixed priors that cannot rapidly adapt to new measurements.

Overall, while manifold learning effectively represents complex motion in low-dimensional spaces, existing approaches are not designed for prospective, ultra-sparse, or online MRI settings, motivating the proposed method.

## 2.2. Prospective MRI Reconstruction

Prospective MRI reconstruction is essential for real-time visualization during interventional and image-guided procedures. By providing clinicians with immediate imaging feedback, for example in MRI-guided radiotherapy, prospective methods can improve targeting accuracy, enhance tumor treatment efficacy, and reduce radiation exposure to surrounding healthy tissues.

Several recent works [13, 16, 25] have explored patient-specific modeling to address this challenge. Liu *et al.* [16] proposed a prior-augmented INR that learns a continuous volumetric representation from only two fully sampled 3D MRIs, enabling sparse 2D cine slices to be lifted into full 3D volumes. Although effective under stable breathing conditions, the method heavily depends on the two static priors, making it sensitive to changes in respiratory patterns. Furthermore, the smoothness bias inherent to the INR formulation limits its ability to represent nonlinear or discontinuous physiological motion, leading to unreliable extrapolation when the motion deviates from the training distribution.

Huttinga *et al.* [13] reconstruct respiratory motion directly from undersampled 3D  $k$ -space by enforcing a low-rank linear motion model. This enables sub-200 ms inference; however, the method assumes that all non-rigid 3D deformations can be expressed as a linear combination of a few fixed spatial bases. Such a linear assumption limits robustness in the presence of nonlinear organ motion or sliding interfaces, where the true deformation cannot be accurately represented by a low-rank linear subspace.

Despite these advances, prospective MRI reconstruction remains largely underexplored. Existing approaches either rely on restrictive priors, impose strong assumptions on motion linearity, or fail to maintain accuracy when motion deviates from the training distribution. Achieving ultra-fast and anatomically reliable volumetric reconstruction therefore remains a critical unmet need in the field.

## 3. Preliminaries

### 3.1. Forward Model of Dynamic MRI

The forward acquisition of dynamic MRI is formulated as:

$$\mathbf{y}_t = \mathbf{P}_t \mathcal{T} \mathbf{x}_t + \mathbf{n}_t, \quad (1)$$

where  $\mathbf{x}_t \in \mathbb{C}^m$  is the image at timestamp  $t$ ,  $\mathcal{T}$  is the Fourier operator,  $\mathbf{P}_t$  is the time-varying sampling pattern, and  $\mathbf{y}_t \in \mathbb{C}^n$  is the acquired  $k$ -space (frequency domain of the image) measurements [11]. To achieve high temporal resolution, the acquisition is typically highly undersampled in the spatial domain (*i.e.*,  $n \ll m$ ). The goal of **retrospective reconstruction** is to recover a high-quality dynamic sequence  $\{\mathbf{x}_t\}_{t=0}^T$  from these undersampled measurements.

### 3.2. Motion-Compensated (MoCo) Reconstruction

MoCo-based methods decompose each dynamic image  $\mathbf{x}_t$  into a time-varying deformation field  $\mathbf{u}_t$  and a static template image  $\mathbf{m}$ , formulated as:

$$\mathbf{x}_t = \mathcal{W}(\mathbf{m}, \mathbf{u}_t), \quad (2)$$

where  $\mathcal{W}(\cdot)$  denotes the image warping operator. The DVF specifies, for each voxel in  $\mathbf{x}_t$ , the displacement vector  $(\Delta x, \Delta y, \Delta z)_t$  that maps it to the corresponding location in the template image space. By leveraging this decomposition, MoCo-based methods transform dynamic reconstruction into estimating the deformation fields with a shared template image. The use of a shared template enables these methods to effectively exploit spatial-temporal correlations [9], allowing high-quality reconstruction even from highly undersampled  $k$ -space data.

### 3.3. Motion-Tracking Guidance Prospective Reconstruction

For prospective reconstruction, the MoCo decomposition is particularly attractive: the template image can be pre-reconstructed using pre-scan data, providing a patient-specific structural prior. Consequently, the prospective reconstruction problem can be reformulated as estimating the current deformation field from the instantaneous  $k$ -space measurement, rather than reconstructing a full 3D image from scratch. The optimization process can be expressed as:

$$\mathbf{u}_{t'}^* = \arg \min_{\mathbf{u}_{t'}} \|\mathbf{y}_{t'} - \mathcal{W}(\mathbf{m}, \mathbf{u}_{t'})\|_2^2 \quad (3)$$

where  $t'$  denotes the new timepoint and  $\mathbf{y}_{t'}$  denotes the instantaneous  $k$ -space measurement.

## 4. Proposed Method

Our goal is to reconstruct high-quality images in a prospective MR acquisition from instantaneous measurements that reflect the object’s current motion state. To achieve this, we propose **PDMR**, which introduces a manifold representation (§ 4.1) to enable fast online motion adaptation. PDMR retrospectively learns a generalizable motion manifold with an effective mapping function from pre-scan dynamic data (§ 4.2). Leveraging the learned manifold and mapping function, PDMR requires optimizing **only a low-dimensional**

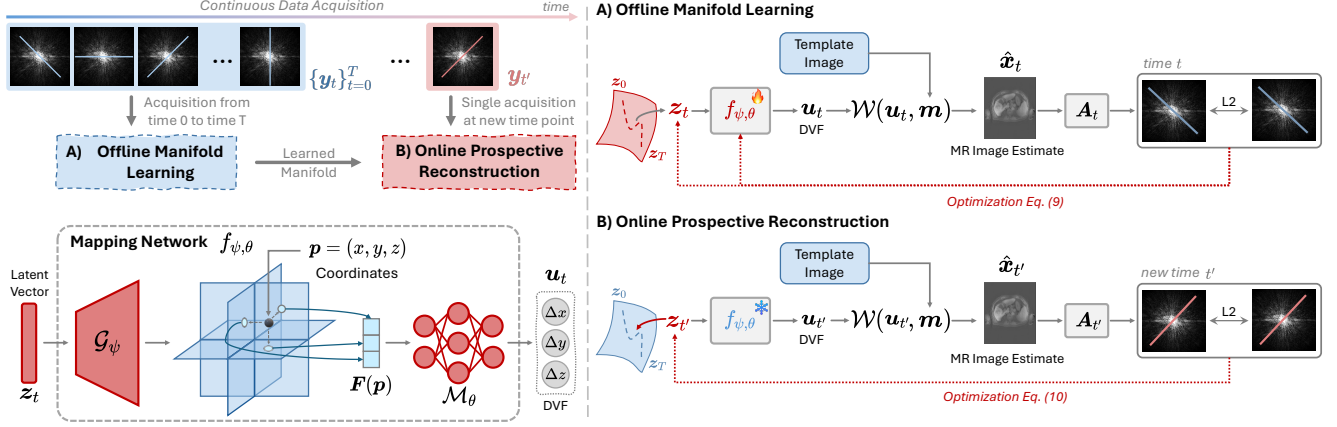


Figure 2. Overview of proposed PDMR. **A.** PDMR performs offline manifold learning, where the patient-specific motion manifold and DVF mapping network  $f_{\psi,\theta}$  are learned from time-continuous sparse measurements  $\{y_t\}_{t=0}^T$  in a retrospective manner. **B.** During online prospective reconstruction, given a single instantaneous measurement  $y_{t'}$ , PDMR rapidly adapts by optimizing only the latent vector while keeping the learned mapping network fixed. Meanwhile, PDMR employs a geometry-aware tri-plane mapping network, enabling the latent vector to be mapped to fine-detailed DVFs efficiently and supporting fast adaptation.

**latent code** to estimate a high-quality deformation field, enabling fast adaptation to new motion states (§ 4.3).

#### 4.1. Manifold-based DVF Representation

Deformation vector fields (DVFs) reflect object movements driven by various physiological signals. To model these complex non-linear mappings, we propose a manifold-based DVF representation that formulates DVF as a function of a low-dimensional latent vector:

$$f: z \in \mathbb{R}^r \mapsto u \in \mathbb{R}^{m \times 3}, \quad (4)$$

where  $z$  encodes the underlying motion state and  $u$  is the corresponding deformation field. To capture fine-grained deformation patterns and ensure efficient computation, we approximate the function  $f$  using a geometry-aware mapping network.

**Geometry-Aware Mapping Network.** Directly mapping the latent code to a full 3D DVF would introduce substantial computational and unstable optimization. Therefore, we adopt a geometry-aware mapping network  $f_{\psi,\theta}$  composed of a tri-plane-based generator  $\mathcal{G}_\psi$  and decoder  $\mathcal{M}_\theta$  to approximate the function  $f$  for accurate DVF estimation, inspired by [4].

Specifically, the tri-plane-based generator  $\mathcal{G}_\psi$  first maps the latent vector  $z$  into three orthogonal feature planes  $\{F_{xy}, F_{xz}, F_{yz}\}$ . Given a spatial coordinate  $p = (x, y, z)$ , its corresponding features are retrieved from the three planes via projection. Then, the geometry-aware feature at  $p$  is obtained by concatenating these three planar features, formulated as:

$$F(p) = F_{xy}(x, y) \oplus F_{xz}(x, z) \oplus F_{yz}(y, z), \quad (5)$$

where  $\oplus$  denotes feature concatenation. Next, the decoder  $\mathcal{M}_\theta$  takes the fused feature as input and predicts the corresponding displacement vector at that position, (*i.e.*,  $\Delta p = \mathcal{M}_\theta(F(p))$ ). Finally, by querying all spatial coordinates in the imaging space  $\Omega$ , we obtain the estimated DVF  $u$  as:

$$u = \{f_{\psi,\theta}(z, p)\}_{p \in \Omega}. \quad (6)$$

#### 4.2. Offline Manifold Learning

Figure 2 (A) shows the overall offline training process. To learn a compact manifold that can represent diverse motions and enable fast adaptation during prospective reconstruction, we jointly optimize latent manifold and network using pre-collected time-continuous measurements  $Y = \{y_t\}_{t=0}^T$  and a template image  $m$ , *e.g.* from the pre-treatment scanning for the specific patient in standard radiotherapy procedure.

Specifically, for each timestep  $t$ , we first sample the latent vector  $z_t$  from a Gaussian distribution, assumed prior distribution. The mapping network then takes the latent vector and imaging spatial coordinates as input to estimate the time-varying DVFs  $\hat{u}_t$  (Eq. 6). Given the estimated DVFs, the template image  $m$  is warped to generate the dynamic image:

$$\hat{x}_t = \mathcal{W}(\hat{u}_t, m), \quad (7)$$

where  $\mathcal{W}(\cdot)$  denotes warping operation. Intergating the forward model of dynamic MRI (Eq. 1), we can get the  $k$ -space estimates as:

$$\hat{Y} = \{A_t \hat{x}_t\}_{t=0}^T, \text{ with } A_t \triangleq P_t \mathcal{T}, \quad (8)$$

Finally, under an auto-decoder formulation [22], both the latent codes and the mapping network are optimized by minimizing the measurement consistency loss together with a

DVF regularization term:

$$\begin{aligned} \mathbf{Z}^*, \psi^*, \theta^* &= \arg \min_{\mathbf{Z}, \psi, \theta} \|\hat{\mathbf{Y}} - \mathbf{Y}\|_2^2 + \lambda \mathcal{R}(\mathbf{U}), \\ \text{where } \mathbf{Z} &= \{\mathbf{z}_t\}_{t=0}^T, \mathbf{U} = \{\mathbf{u}_t\}_{t=0}^T, \end{aligned} \quad (9)$$

where  $\mathcal{R}(\cdot)$  denotes the DVF regularization term that enforces temporal smoothness, and  $\lambda$  is the weighting hyper-parameter.

### 4.3. Online Prospective Reconstruction

After completing the offline manifold learning stage, we obtain a compact manifold and a well-trained mapping network to capture patient-specific motion representations through retrospective training. Given a random sample from this manifold, the mapping network is able to generate fine-grained spatio-temporal deformation patterns. Therefore, in the online prospective reconstruction, we freeze the parameters  $(\psi^*, \theta^*)$  of the mapping network and optimize only the latent vector  $\mathbf{z}$  corresponding to the current time frame.

Specifically, given an instantaneous measurement  $\mathbf{y}_{t'}$ , the latent vector  $\mathbf{z}_{t'}$  is optimized within the learned manifold by minimizing the discrepancy between the estimated and acquired  $k$ -space data. The optimization process can be formulated as:

$$\begin{aligned} \mathbf{z}_{t'} &= \arg \min_{\mathbf{z}} \|\mathbf{A}_{t'} \mathbf{x}_{t'} - \mathbf{y}_{t'}\|_2^2, \\ \text{with } \mathbf{x}_{t'} &= \mathcal{W}(\mathbf{m}, \mathbf{f}_{\psi^*, \theta^*}(\mathbf{z})). \end{aligned} \quad (10)$$

Once the optimal latent vector  $\hat{\mathbf{z}}_{t'}$  is obtained, the corresponding DVF  $\hat{\mathbf{u}}_{t'} = f_{\psi, \theta}(\hat{\mathbf{z}}_{t'})$  is used to warp the template image  $\mathbf{m}$  to generate the current frame:

$$\hat{\mathbf{x}}_{t'} = \mathcal{W}(\mathbf{m}, \hat{\mathbf{u}}_{t'}). \quad (11)$$

This procedure enables ultra-fast motion tracking and prospective reconstruction. Since only a low-dimensional latent vector needs to be optimized per time frame, the inference process is highly efficient and can rapidly adapt to unseen motion states while preserving the physical plausibility encoded in the learned manifold.

## 5. Experiments & Results

### 5.1. Datasets and Preprocessing

**XCAT Phantom Data.** We used digital XCAT phantoms [24] with simulated respiratory motion in the abdominal region, where the parameter maps were assigned based on previous literature [6] and the dynamic 3D data were simulated using a spoiled gradient echo sequence configured with the same acquisition parameters as our in-house protocol, serving as ground-truth reference data. Each respiratory cycle lasted 3.97 seconds, and the dynamic sequence was simulated with a temporal resolution of 170 ms per frame.

**In-house Data.** In-house data were acquired from six subjects under an institutional review board (IRB)-approved protocol. A 10-min DCE-MRI scan was performed using a work-in-progress golden-angle stack-of-stars radial trajectory, yielding 3500 spokes (170 ms per spoke acquisition). Using the hierarchical motion modeling framework [31], we extracted respiratory motion signals by analyzing the liver’s center-of-mass trajectory, and used these signals to bin the data and reconstruct 21 respiratory-resolved 3D volumes. Each volume was deformably registered to the end-exhale reference to obtain DVFs for all 21 respiratory states. Per-spoke DVFs were computed via linear interpolation between the bounding respiratory states based on its continuous respiratory position. By applying these DVFs to the reference volume, we generated high-temporal-resolution dynamic 3D MRI datasets, which serve as ground truth.

**Simulated Acquisition Process.** For both the XCAT phantom and the six in-house dynamic 3D MRI datasets, we employed a golden-angle stack-of-stars sampling pattern, acquiring only one stack of spokes per time frame. Each spoke consisted of 448 readout samples with  $k_z = 96$  partitions. Spokes 0–150 were used for offline manifold learning, while prospective reconstruction was evaluated using spokes 150–300 and 1000–1150. Since each spoke corresponds to approximately 170 ms, the latter interval reflects data acquired roughly 2 minutes after the initial acquisition.

### 5.2. Baselines & Metrics

**Baselines.** We compare PDMR with six representative dynamic MRI reconstruction approaches:

- 1) Analytical algorithms: **NUFFT** [12] performs non-Cartesian reconstruction using the non-uniform FFT; **GRASP** [10] applies compressed-sensing constraints under golden-angle sampling to jointly reconstruct the dynamic sequence retrospectively;
- 2) Retrospective methods: **TDDIP** [30] extends Deep Image Prior [29] to dynamic imaging by fitting a CNN generator to the full temporal measurements; **SPINER** [5] uses an implicit neural representation to model the dynamic volume as a continuous function of space and time;
- 3) Prospective methods: **Prior-INR** [16] employs a hand-crafted discrete motion manifold; **MR-MOTUS** [13] updates motion in a linear subspace using sequential  $k$ -space measurements.

**Evaluation Metrics.** For the reconstructed dynamic MRI, we employ peak signal-to-noise ratio (PSNR) and structural similarity index (SSIM) as quantitative evaluation metrics.

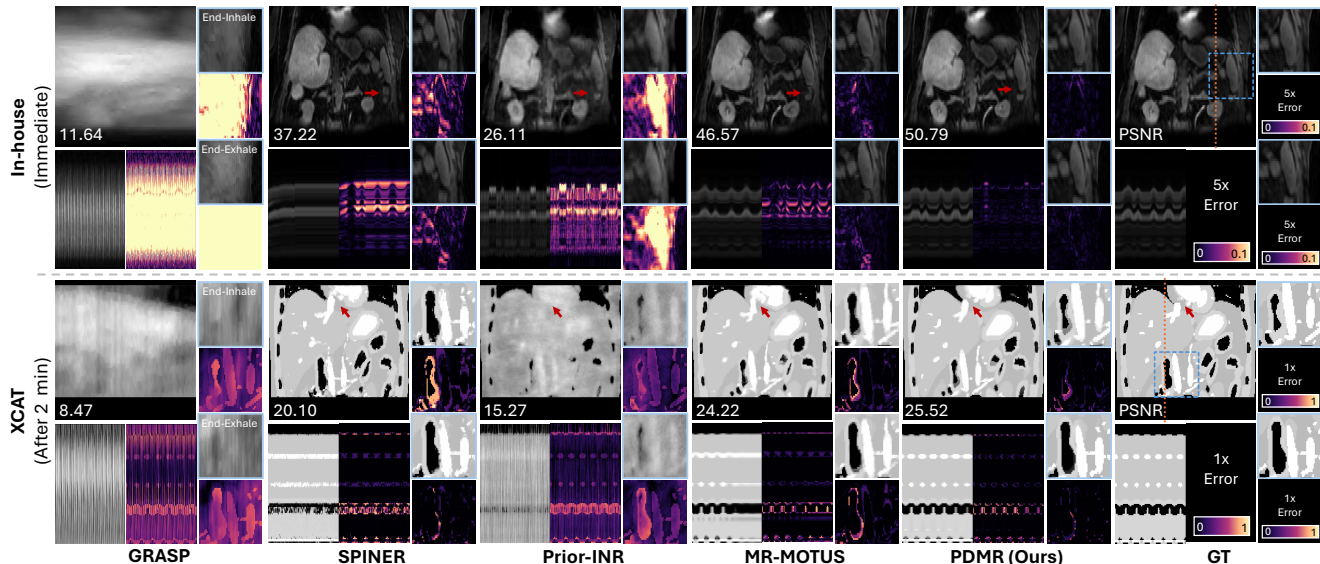


Figure 3. Qualitative comparisons of prospective reconstruction results on the in-house dataset (top row) and the XCAT dataset (bottom row). We display the reconstructed images, the over-time profile lines in the  $z-t$  plane, and the corresponding error maps. The selected  $z$ -axis location is marked by an orange dashed line, and zoom-in boxes highlight regions of interest at the end-inhale and end-exhale motion states for improved visualization of motion capture. Red arrows indicate noticeable small-motion capture failures in the baselines.

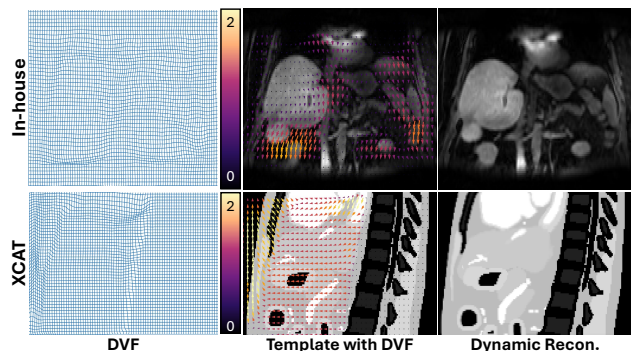


Figure 4. Visualization of the estimated DVFs during prospective reconstruction on the in-house dataset (coronal view) and the XCAT dataset (sagittal view).

### 5.3. Implementation Details

In PDMR, the latent code dimension is set to  $r = 12$ , and each tri-plane contains 32 feature channels. The mapping network is composed of a tri-plane encoder followed by a lightweight MLP decoder (See implementation details in the supplementary). Offline training is performed using the Adam optimizer, with learning rates of  $1 \times 10^{-2}$  for the mapping network and  $5 \times 10^{-3}$  for the latent vectors, and is run for 50 iterations. All models were implemented in PyTorch and trained on an NVIDIA A100 GPU. Detailed inference time analysis is provided in the supplementary material.

### 5.4. Prospective Reconstruction

**Experimental Settings.** To evaluate the effectiveness of PDMR for prospective reconstruction, we conduct experiments on both XCAT phantoms and in-house abdominal MRI data under two prospective settings: 1) **Immediate**: the prospective acquisition starts immediately after the retrospective scan. 2) **After 2 min**: where a two-minute interval separates the retrospective and prospective acquisitions.

In all experiments, the analytical algorithms are directly evaluated under the prospective reconstruction setting. Both the prospective methods and the retrospective baselines are first trained on the retrospective data, and then adapted to the newly acquired measurements during the prospective stage. We compare the dynamic MR reconstruction performance of all baselines in the prospective scenario. Additional implementation details, parameter settings, and evaluation protocols are provided in the supplement.

**Comparisons of Reconstructed MR images.** Figure 3 shows the quantitative results. The analytical method GRASP results in highly blurred images, losing all anatomical details, highlighting the failure of traditional methods with ultra-sparse measurements in the latency window. For retrospective methods, SPINER [5] fails to generalize to unseen time points. It tends to extrapolate past motion trends and eventually produces nearly static outputs when evaluated at new timestamps, indicating its limited ability for prospective reconstruction. For the prospective methods, Prior-INR [16], which relies on a hand-crafted and discrete

Category	Method	XCAT Phantom		In-house Data	
		Immediate	After 2 min	Immediate	After 2 min
Analytical	NUFFT [12]	7.80/0.252	7.79/0.252	10.89±0.53/0.364±0.022	10.90±0.52/0.365±0.021
	GRASP [10]	8.47/0.158	8.47/0.158	10.89±0.60/0.120±0.017	11.05±0.88/0.126±0.027
Retrospective Recon.	TDDIP [30]	17.73/0.498	18.05/0.552	25.38±1.84/0.661±0.044	25.70±2.81/0.687±0.068
	SPINER [5]	20.25/0.873	20.10/0.869	35.43±1.89/0.942±0.018	36.36±3.40/0.946±0.022
Prospective Recon.	Prior-INR [16]	15.05/0.444	15.27/0.473	26.72±2.46/0.810±0.087	27.00±2.76/0.811±0.087
	MR-MOTUS [13]	24.39/0.931	24.22/0.929	41.04±3.41/0.981±0.007	41.11±3.50/0.976±0.011
	<b>PDMR (Ours)</b>	<b>26.28/0.958</b>	<b>25.52/0.950</b>	<b>46.32±4.06/0.994±0.003</b>	<b>43.39±4.58/0.978±0.023</b>

Table 1. Quantitative results (PSNR (dB)/SSIM) of compared methods on the XCAT phantom and in-house datasets under immediate and 2-minute delayed prospective reconstruction settings. The best results are highlighted in **bold**.

manifold, also exhibits noticeable limitations. As shown in the  $z-t$  profile, the learned motion trajectories are discontinuous and fail to reflect the smooth and continuous nature of physiological motion, leading to inaccurate deformation estimation during prospective reconstruction. MR-MOTUS shows better motion tracking, but still exhibits noticeable errors, which are particularly evident in the  $z-t$  profile error comparison. Additionally, due to its linear representation limitations, MR-MOTUS struggles to capture small motions, as highlighted with red arrows in the figure. In contrast, PDMR achieves near-perfect alignment with the ground truth, accurately capturing both large-scale motion and fine local dynamics, demonstrating its superior ability to model complex deformation patterns with high fidelity.

Table 1 presents the quantitative results. PDMR outperforms all baselines in both settings across XCAT Phantom and in-house data, showing a significant improvement over the SOTA MR-MOTUS (*e.g.*,  $\sim 2$ dB gain on in-house data). These results demonstrate that PDMR consistently provides more accurate and reliable reconstructions, highlighting its superior performance in prospective reconstructions across diverse acquisition conditions.

### 5.5. Evaluation of PDMR’s Effectiveness

We evaluated PDMR’s performance in both offline learning from retrospective data and prospective adaptation of DVFs.

**Evaluation of Offline Learning.** Table 2 shows the performance of PDMR on retrospective data compared with baselines. It outperforms advanced retrospective methods, demonstrating its ability to effectively learn motion dynamics and capture detailed deformation fields from undersampled data.

**Evaluation of DVFs.** Figure 4 shows the estimated DVFs alongside the dynamic reconstruction results in the prospective setting. The quiver plots (second column) visualize

Method	XCAT	In-house
TDDIP [30]	17.21/0.372	25.93±2.07/0.582±0.058
SPINER [5]	21.26/0.888	38.14±4.40/0.954±0.031
MR-MOTUS [13]	25.72/0.948	43.50±4.81/0.986±0.010
<b>PDMR (Ours)</b>	<b>26.63/0.959</b>	<b>47.60±3.44/0.995±0.002</b>

Table 2. Quantitative results (PSNR (dB)/SSIM) of compared methods on the XCAT phantom and in-house datasets during retrospective learning. The best results are highlighted in **bold**.

the direction and magnitude of the predicted DVFs, which closely follow the expected organ motion patterns, demonstrating that our method accurately captures respiratory dynamics. Notably, for regions that remain stationary (such as the spine in the XCAT phantom) our method preserves the absence of motion, demonstrating that the learned deformation manifold does not introduce spurious displacements in anatomically static structures. Additional visual results are provided in the supplementary material.

## 6. Discussion

In this section, we analyze the interpretability and representativeness of the learned latent vector in PDMR (§ 6.1). Meanwhile, we analyze the PDMR’s ability to generalize to unseen motion in prospective reconstruction (§ 6.2).

### 6.1. Analysis of Latent Vector

To demonstrate the interpretability of the latent vector, we perform PCA on the latent vectors  $z$  learned offline and adapted during prospective reconstruction. We extract the first principal component (PC) and compare it with the reference respiratory motion signal, which represents the superior-inferior displacement of the liver, shown in Figure 6. Despite small perturbations, the first PC of the latent code exhibits a clear correlation with the motion signal which indicates that the latent code learned by PDMR captures

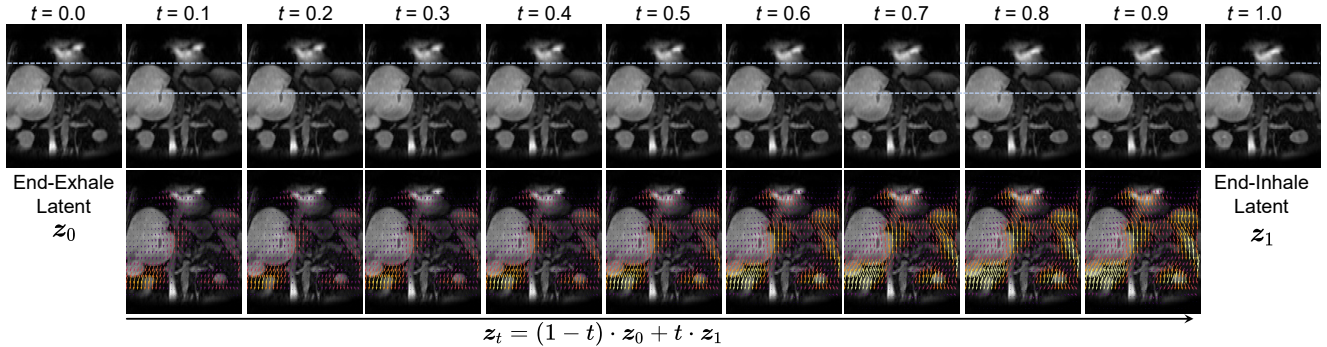


Figure 5. Visualization of reconstructed MR images and corresponding DVFs obtained from interpolating between two latent vectors, where  $z_0$  and  $z_1$  denote the learned vectors at the inhale and exhale motion states. The dashed line highlights the respiratory-induced displacement for clearer visualization.

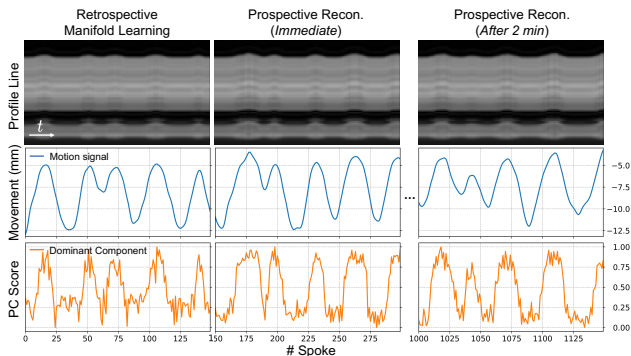


Figure 6. Visualization comparing the representative profile line ( $z-t$  plane), the reference diaphragm motion, and the first principal component (PC) of the latent vector  $z$  in both retrospective and prospective reconstructions.

motion-related variations effectively.

To demonstrate that the learned manifold is continuous and physiologically reasonable, as well as to assess the generalization capability of the mapping network, we interpolate between latent vectors corresponding to the inhale and exhale respiratory states and decode them using the trained network. Specifically, we denote the latent vector at the end-inhale state as  $z_0$  and at the end-exhale state as  $z_1$ . Intermediate latent vectors are generated through linear interpolation at uniform steps of 0.1 ( $t = 0.1, \dots, 0.9$ ), with the reconstructed images shown in Figure 5 (top row). The highlighted horizontal lines visualize the inferred respiratory displacement, which varies smoothly with the interpolated latent vectors. The corresponding template images and DVFs are displayed in the bottom row of Figure 5, and the consistent linear progression in the DVFs further indicates that the latent space encodes a continuous, structured representation of respiratory motion. Additional analysis is provided in the supplementary material.

Offset	0 mm	1 mm	2 mm	3 mm
PSNR (dB)	52.53	44.65	40.63	38.80
SSIM	0.998	0.991	0.978	0.964

Table 3. Qualitative results of PDMR with unseen motion patterns with different additional motion offsets.

## 6.2. Robustness on Unseen Motion State

To explore the performance of PDMR under unseen motion patterns, we introduce additional respiratory displacements (0–3 mm in the vertical direction) during prospective reconstruction and the quantitative result is shown in Table 3. The reconstruction quality gradually decreases as the displacement increases; however, even with a 3 mm offset, which is well outside the range observed during offline training, PDMR still achieves 38.80 dB PSNR, demonstrating strong robustness to unseen motion.

## 7. Conclusion

In this work, we introduced PDMR, a manifold-based framework for prospective dynamic 3D MRI reconstruction from single measurements. PDMR retrospectively learns a compact and temporally generalizable motion manifold with a geometry-aware tri-plane mapping network, enabling high-fidelity deformation modeling. During online reconstruction, it efficiently adapts to new motion states by optimizing only a low-dimensional latent code, achieving accurate DVF estimation within a few iterations. Experiments on XCAT phantoms and in-house datasets show that PDMR outperforms SOTA methods, providing higher reconstruction fidelity, smoother motion trajectories, and stronger robustness to unseen motion. These results demonstrate the potential of manifold-based deformation modeling for real-time, motion-aware MRI guidance.

**Acknowledgment.** This work was partially supported by NIH R01EB032825 and Siemens Healthineers NIH/NHLBI R01HL163030. LS acknowledges funding support by National Science Foundation via grant IIS-2435746, Defense Advanced Research Projects Agency under contract No. HR00112520042. We thank Xuanyu Tian for insightful discussions and valuable assistance in the preparation of this manuscript.

## References

- [1] Marcel Beetz, Jorge Corral Acero, Abhirup Banerjee, Ingo Eitel, Ernesto Zacur, Torben Lange, Thomas Stiermaier, Ruben Evertz, Sören J Backhaus, Holger Thiele, et al. Interpretable cardiac anatomy modeling using variational mesh autoencoders. *Frontiers in Cardiovascular Medicine*, 9: 983868, 2022. 2
- [2] Mikhail Belkin and Partha Niyogi. Laplacian eigenmaps for dimensionality reduction and data representation. *Neural computation*, 15(6):1373–1396, 2003. 2
- [3] Tom Brosch, Roger Tam, and Alzheimer’s Disease Neuroimaging Initiative. Manifold learning of brain mris by deep learning. In *International Conference on Medical Image Computing and Computer-Assisted Intervention*, pages 633–640. Springer, 2013. 2
- [4] Eric R Chan, Connor Z Lin, Matthew A Chan, Koki Nagano, Boxiao Pan, Shalini De Mello, Orazio Gallo, Leonidas J Guibas, Jonathan Tremblay, Sameh Khamis, et al. Efficient geometry-aware 3d generative adversarial networks. In *Proceedings of the IEEE/CVF Conference on Computer Vision and Pattern Recognition*, pages 16123–16133, 2022. 2, 4
- [5] Lixuan Chen, James M Balter, Liyue Shen, and Jeong Joon Park. Single-spoke motion-compensated dynamic 3d mri reconstruction via neural representation. In *International Conference on Medical Image Computing and Computer-Assisted Intervention*, pages 513–522. Springer, 2025. 1, 5, 6, 7
- [6] Yong Chen, Yun Jiang, Shivani Pahwa, Dan Ma, Lan Lu, Michael D Twieg, Katherine L Wright, Nicole Seiberlich, Mark A Griswold, and Vikas Gulani. Mr fingerprinting for rapid quantitative abdominal imaging. *Radiology*, 279(1): 278–286, 2016. 5
- [7] Ronald R Coifman and Stéphane Lafon. Diffusion maps. *Applied and Computational Harmonic Analysis*, 21(1):5–30, 2006. 2
- [8] Jie Feng, Ruimin Feng, Qing Wu, Xin Shen, Lixuan Chen, Xin Li, Li Feng, Jingjia Chen, Zhiyong Zhang, Chunlei Liu, et al. Spatiotemporal implicit neural representation for unsupervised dynamic mri reconstruction. *IEEE Transactions on Medical Imaging*, 40(5):2143–2156, 2025. 3
- [9] Li Feng, Thomas Benkert, Kai Tobias Block, Daniel K Sodickson, Ricardo Otazo, and Hersh Chandarana. Compressed sensing for body mri. *Journal of Magnetic Resonance Imaging*, 45(4):966–987, 2017. 3
- [10] Li Feng, Qiuting Wen, Chenchan Huang, Angela Tong, Fang Liu, and Hersh Chandarana. Grasp-pro: improving grasp dce-mri through self-calibrating subspace-modeling and contrast phase automation. *Magnetic Resonance in Medicine*, 83(1):94–108, 2020. 1, 5, 7
- [11] Jeffrey A Fessler. Model-based image reconstruction for mri. *IEEE Signal Processing Magazine*, 27(4):81–89, 2010. 3
- [12] Jeffrey A Fessler and Bradley P Sutton. Nonuniform fast fourier transforms using min-max interpolation. *IEEE Transactions on Signal Processing*, 51(2):560–574, 2003. 5, 7
- [13] Niek RF Huttinga, Tom Bruijnen, Cornelis AT Van Den Berg, and Alessandro Sbrizzi. Real-time non-rigid 3d respiratory motion estimation for mr-guided radiotherapy using mr-motus. *IEEE Transactions on Medical Imaging*, 41(2):332–346, 2021. 2, 3, 5, 7
- [14] Paul J Keall, Caterina Brighi, Carri Glide-Hurst, Gary Liney, Paul ZY Liu, Suzanne Lydiard, Chiara Paganelli, Trang Pham, Shanshan Shan, Alison C Tree, et al. Integrated mri-guided radiotherapy—opportunities and challenges. *Nature Reviews Clinical Oncology*, 19(7):458–470, 2022. 1
- [15] Diederik P Kingma and Max Welling. Auto-encoding variational bayes. In *International Conference on Learning Representations*, 2014. 2
- [16] Lianli Liu, Liyue Shen, Adam Johansson, James M Balter, Yue Cao, Lucas Vitzthum, and Lei Xing. Volumetric mri with sparse sampling for mr-guided 3d motion tracking via sparse prior-augmented implicit neural representation learning. *Medical Physics*, 51(4):2526–2537, 2024. 2, 3, 5, 6, 7
- [17] Ben Mildenhall, Pratul P Srinivasan, Matthew Tancik, Jonathan T Barron, Ravi Ramamoorthi, and Ren Ng. Nerf: Representing scenes as neural radiance fields for view synthesis. *Communications of the ACM*, 65(1):99–106, 2021. 3
- [18] Manuel A. Morales, David Izquierdo-Garcia, Iman Aganj, Jayashree Kalpathy-Cramer, Bruce R. Rosen, and Ciprian Catana. Implementation and validation of a three-dimensional cardiac motion estimation network. *Radiology: Artificial Intelligence*, 1(4):e180080, 2019. 2
- [19] Krishna S Nayak, Yongwan Lim, Adrienne E Campbell-Washburn, and Jennifer Steeden. Real-time magnetic resonance imaging. *Journal of Magnetic Resonance Imaging*, 55(1):81–99, 2022. 1
- [20] Jiazhen Pan, Daniel Rueckert, Thomas Küstner, and Kerstin Hammernik. Learning-based and unrolled motion-compensated reconstruction for cardiac mr cine imaging. In *International Conference on Medical Image Computing and Computer-Assisted Intervention*, pages 686–696. Springer, 2022. 2
- [21] Jiazhen Pan, Wenqi Huang, Daniel Rueckert, Thomas Küstner, and Kerstin Hammernik. Motion-compensated mr cine reconstruction with reconstruction-driven motion estimation. *IEEE Transactions on Medical Imaging*, 43(7): 2420–2433, 2024. 2
- [22] Jeong Joon Park, Peter Florence, Julian Straub, Richard Newcombe, and Steven Lovegrove. DeepSDF: Learning continuous signed distance functions for shape representation. In *Proceedings of the IEEE/CVF Conference on Computer Vision and Pattern Recognition*, pages 165–174, 2019. 3, 4

- [23] Sam T Roweis and Lawrence K Saul. Nonlinear dimensionality reduction by locally linear embedding. *Science*, 290(5500):2323–2326, 2000. [2](#)
- [24] W Paul Segars, G Sturgeon, S Mendonca, Jason Grimes, and Benjamin MW Tsui. 4d xcat phantom for multimodality imaging research. *Medical Physics*, 37(9):4902–4915, 2010. [2](#), [5](#)
- [25] Hua-Chieh Shao, Xiaoxue Qian, Guoping Xu, Can Wu, Ricardo Otazo, Jie Deng, and You Zhang. A dynamic reconstruction and motion estimation framework for cardiorespiratory motion-resolved real-time volumetric mr imaging (dreme-mr). *Physics in Medicine and Biology*, 70(17):175013, 2025. [2](#), [3](#)
- [26] Liyue Shen, John Pauly, and Lei Xing. Nerp: implicit neural representation learning with prior embedding for sparsely sampled image reconstruction. *IEEE Transactions on Neural Networks and Learning Systems*, 35(1):770–782, 2022. [3](#)
- [27] Vincent Sitzmann, Julien Martel, Alexander Bergman, David Lindell, and Gordon Wetzstein. Implicit neural representations with periodic activation functions. *Advances in Neural Information Processing Systems*, 33:7462–7473, 2020. [3](#)
- [28] Xuanyu Tian, Lixuan Chen, Qing Wu, Xiao Wang, Jie Feng, Yuyao Zhang, and Hongjiang Wei. Unsupervised motion-compensated decomposition for cardiac mri reconstruction via neural representation. In *Proceedings of the AAAI Conference on Artificial Intelligence*, pages 9529–9537, 2026. [2](#)
- [29] Dmitry Ulyanov, Andrea Vedaldi, and Victor Lempitsky. Deep image prior. In *Proceedings of the IEEE Conference on Computer Vision and Pattern Recognition*, pages 9446–9454, 2018. [5](#)
- [30] Jaejun Yoo, Kyong Hwan Jin, Harshit Gupta, Jerome Yerly, Matthias Stuber, and Michael Unser. Time-dependent deep image prior for dynamic mri. *IEEE Transactions on Medical Imaging*, 40(12):3337–3348, 2021. [1](#), [5](#), [7](#)
- [31] Yuhang Zhang, Rojano Kashani, Yue Cao, Theodore S Lawrence, Adam Johansson, and James M Balter. A hierarchical model of abdominal configuration changes extracted from golden angle radial magnetic resonance imaging. *Physics in Medicine and Biology*, 66(4):045018, 2021. [5](#)